ADVANCED PHOTONICS RESEARCH Open Access
www.adpr-journal.com

High-Performance Single-Crystal Diamond Detector for Accurate Pulse Shape Discrimination Based on Self-Organizing Map Neural Networks

Guang-Wei Huang, Zhi-Yuan Li, Zun-Gang Wang, Wu-Rui Song, Kun Wu, Lin-Xiang Li, Chun-Zhi Zhou, Yi-Yun Zhang,* Zhi-Qiang Liu, Xiao-Yan Yi, and Jin-Min Li*

Herein, a high-performance single-crystal diamond (SCD) detector ($4.5 \times 4.5 \times 0.3\ mm^3$) to achieve accurate pulse shape discrimination, which is critical for source tracking in harsh and complex radiation conditions, is demonstrated. Enabled by a deep learning algorithm based on self-organizing map (SOM) neural networks, and using the transient current technique (TCT) for sampling the detector's response to γ, α, and neutron radiation fields, the SCD detector achieves high recognition accuracy of 97.51%. The SCD detector exhibits a low leakage current of $0.75\ pA\ mm^{-2}$ under an electric field of $0.51\ V\ \mu m^{-1}$, and its response to ^{238}Pu α-rays shows that the charge collection efficiency for electrons and holes is as high as 99.2 and 98.8% respectively, with an energy resolution as low as 1.42%. The results indicate that the high-performance SCD detector assisted by the machine learning algorithm can effectively distinguish α-particles and γ-rays with a potential application in separating the neutron and γ events as well.

1. Introduction

The extraordinary properties of diamond, such as ultrawide bandgap ($\approx$5.5 eV), radiation hardness, high resistivity, and high carrier mobility, make it an ideal material for robust radiation detectors yet with a simple structure.[1–4] In recent years, the quality of chemical vapor deposition (CVD) single-crystal diamond (SCD) has been greatly improved,[5] which makes SCD detectors possible in counting and spectroscopy applications. At present, SCD detectors are widely used in fusion experiments, medical, and fission reactor applications, which are emerging as next-generation semiconductor radiation detectors with great potential.[6] Due to the extremely high resistivity of the diamond film[7] (usually $> 10^{12}\ \Omega\ cm$), the device configuration of the SCD detector is simple, not requiring p–n junctions for low leakage current as any other counterpart.[8,9] In general, the SCD detector utilizes a vertical "sandwich" layout of a metal–semiconductor–metal (MSM) structure with low capacitance, fast response, and low noise.[10] The physical mechanism of SCD detectors is similar to that of other semiconductor detectors, operated by generating current out of ionizing radiation.[11] SCD detectors therefore can be used to measure α-particles, electrons,[12] X-rays, γ-rays,[13] and neutrons.[14] However, these applications rely on the high performance of the detector, in which charge collection efficiency (CCE), energy resolution, and time response are the three leading criteria to evaluate the performance of SCD detectors. The detector's performance greatly depends on the properties of the diamond.[15,16] In addition, accurate neutron monitoring in high-radiation flux of the fission and fusion reactors[17,18] requires algorithms that can distinguish the signals of interests from the background. As SCD detectors are sensitive to γ-rays, it is necessary in these applications to distinguish neutrons from γ-rays background. In fact, high-energy neutron radiation would induce "point-like" ionizations over the entire volume of the SCD, as heavily charged products of the nuclear reaction are greatly localized with their short range. However, this is different from the effects caused by the incident γ-rays. When the MeV

G.-W. Huang, Z.-Y. Li, Z.-G. Wang, K. Wu, L.-X. Li, C.-Z. Zhou
State Key Laboratory of NBC Protection for Civilian
Beijing 102205, P. R. China
E-mail: zhoucz6622@163.com

G.-W. Huang, W.-R. Song, Y.-Y. Zhang, Z.-Q. Liu, X.-Y. Yi, J.-M. Li
Research and Development Center for Solid State Lighting
Institute of Semiconductors
Chinese Academy of Sciences
Beijing 100083, P. R. China
E-mail: yyzhang@semi.ac.cn

W.-R. Song, Y.-Y. Zhang, Z.-Q. Liu, X.-Y. Yi, J.-M. Li
Center of Materials Science and Optoelectronics Engineering
University of Chinese Academy of Sciences
Beijing 100190, P. R. China

The ORCID identification number(s) for the author(s) of this article can be found under https://doi.org/10.1002/adpr.202100138.

© 2021 The Authors. Advanced Photonics Research published by Wiley-VCH GmbH. This is an open access article under the terms of the Creative Commons Attribution License, which permits use, distribution and reproduction in any medium, provided the original work is properly cited.

DOI: 10.1002/adpr.202100138

energy γ-rays from the background interact with the ^{12}C atoms in the SCD, they generate Compton electrons due to the low atomic mass of ^{12}C. The Compton electrons would range widely over a few millimeters in ^{12}C, which is much larger than the device thickness. As a result, these penetrative "track-like" ionizations occur homogeneously when γ-rays from the background interact with the SCD.[19] It is important to note that the shape of the readout pulse is defined by these unique characteristic initial ionization profiles, which enables pulse shape discrimination. In this regard, full width at half maximum (FWHM) of the response pulses has been used as a main characteristic for the rejection of γ-ray background from charged-particle spectra.[20] By computing triangularity, pulse shape discrimination of neutrons and γ-rays has been already reported, whereas it is limited to a particular class of neutrons that hit the ballistic center of the detector.[19] Moreover, Passeri et al. presented four neutron/γ-ray separation algorithms for SCD detectors, three of which rely on pulse shape information and one on the frequency analysis.[21] Nevertheless, all the earlier algorithms require a priori knowledge, as well as high-quality data for accurate discrimination, which limit their further applications. Hence, unsupervised machine learning classification algorithms are needed for more accurate and detailed numerical analysis in particle identification. In this regard, the self-organizing map (SOM) algorithm is a simplified single-layer neural network with a topology proposed by Kohonen, which can virtually be applied on any type of data.[22] In addition, without any prior knowledge about the data, SOM algorithm can efficiently create classifications while retaining topological information about similarity among classes. Therefore, SOMs can be developed with any desired level of details—the fact that makes them particularly suitable for clustering data in many dimensions with varying degrees of complexity in shaped and connected feature spaces.[23] In this article, we first report the fabrication process and related test results of the high-performance SCD detector. A deep learning algorithm based on SOM neural networks for pulse shape discrimination is then developed to realize accurate tracking of complex radiation fields. The accuracy of the proposed approach benefiting from the good performance and fast response of SCD detector and accurate transient current technique (TCT) was verified by identification of n/γ and α/γ events experimentally.

2. Results and Discussion

A piece of Element-six (E6) electronic-grade SCD ($4.5 \times 4.5 \times 0.3\,mm^3$) was used in this work. The as-grown SCD for detector processing exhibited excellent surface morphology, as measured by atomic force microscopy (AFM), with a root-mean-square (RMS) roughness of 3.9 Å over an area of $20 \times 20\,\mu m^2$. High-resolution X-ray diffraction diamond (111) peak at 43.9° exhibits an FWHM of 139 arcsec (see Figure S1, S2, Supporting Information). **Figure 1** shows the Raman spectra of SCD using a 532 nm pulse laser as the excitation source. The signature sp^3 peak is at $1331.5\,cm^{-1}$ with an FWHM of $1.85\,cm^{-1}$. No other impurity (sp^2, graphite) peaks in the Raman spectra were observed, which confirmed that the SCD material was well crystallized with a low internal stress and defect density. Inset of Figure 1 shows the schematic diagram of the

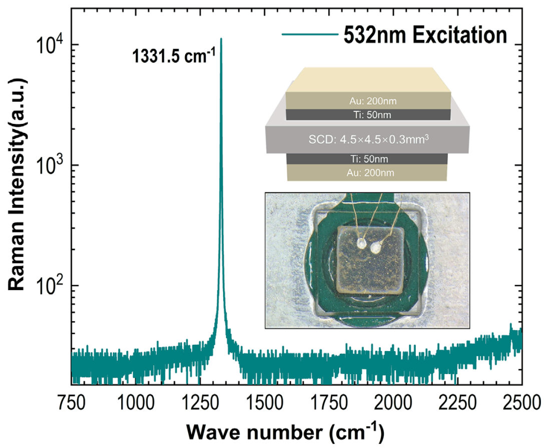

Figure 1. Raman spectra of an SCD. Inset shows the schematic diagram of the SCD detector structure and as-fabricated device for test.

SCD detector structure and the as-fabricated device for test. **Figure 2**a shows the dark I–V characteristics of the SCD detector. The dark current density is about $0.75\,pA\,mm^{-2}$ at a forward bias of 154 V, when the SCD detector exhibits the peak CCE under α-particle radiation. In addition, a marginally higher dark current with the increase in bias voltage at the positive polarity can be observed, which indicates a polarity-dependent signature of a rise in the leakage current. It implies that the SCD may still have impurities or shallow-level traps with it, such as nitrogen-related defects produced during the growth of the SCD,[24] and they can release free charges over a certain high field, eventually causing a sharp rise in current. As the SCD detector device was exposed to the ^{238}Pu α-particle source, the carriers were created near the upper electrode. These carriers (either electrons or holes) would drift to the bottom electrode driven by the electric field applied on the SCD detector. As a result, neglecting the trapping or scattering, if any, a square-shape signal would be generated when the carriers reach the farthest electrode. The shape of the current pulse greatly depends on the electric field and properties of the material under test. Bias-dependent time-resolved pulse response for electrons and holes drift is shown in Figure 2b,c. The response pulses get sharper and then saturate as the electric field increases to $1.67\,V\,\mu m^{-1}$ and beyond, which is mainly caused by the incomplete charge collection at low-electric field conditions. The rise/decay time are about 470 ps/469 ps for holes and 522 ps/470 ps for electrons at $1.67\,V\,\mu m^{-1}$, respectively (see Figure S4, Supporting Information). The measured voltage $V(t)$ can be converted to collected charges Q by the following equation.

$$Q = \int_{t_{start}}^{t_{end}} i(t)\mathrm{d}t \qquad i(t) = \frac{1}{A_{amp}R_{in}}\left[R_{in}C_d\frac{\mathrm{d}V(t)}{\mathrm{d}t} + V(t)\right] \tag{1}$$

where t_{start} and t_{end} are defined as the time when the current signal rises above and decays below a threshold level respectively, whereas A_{amp} and R_{in} are the two parameters calibrated by the amplifier. According to Equation (1), it can be found that the collected charge basically saturates beyond an electric field of $0.5\,V\,\mu m^{-1}$. In this situation, field carrier mobility for electrons

© 2021 The Authors. Advanced Photonics Research published by Wiley-VCH GmbH

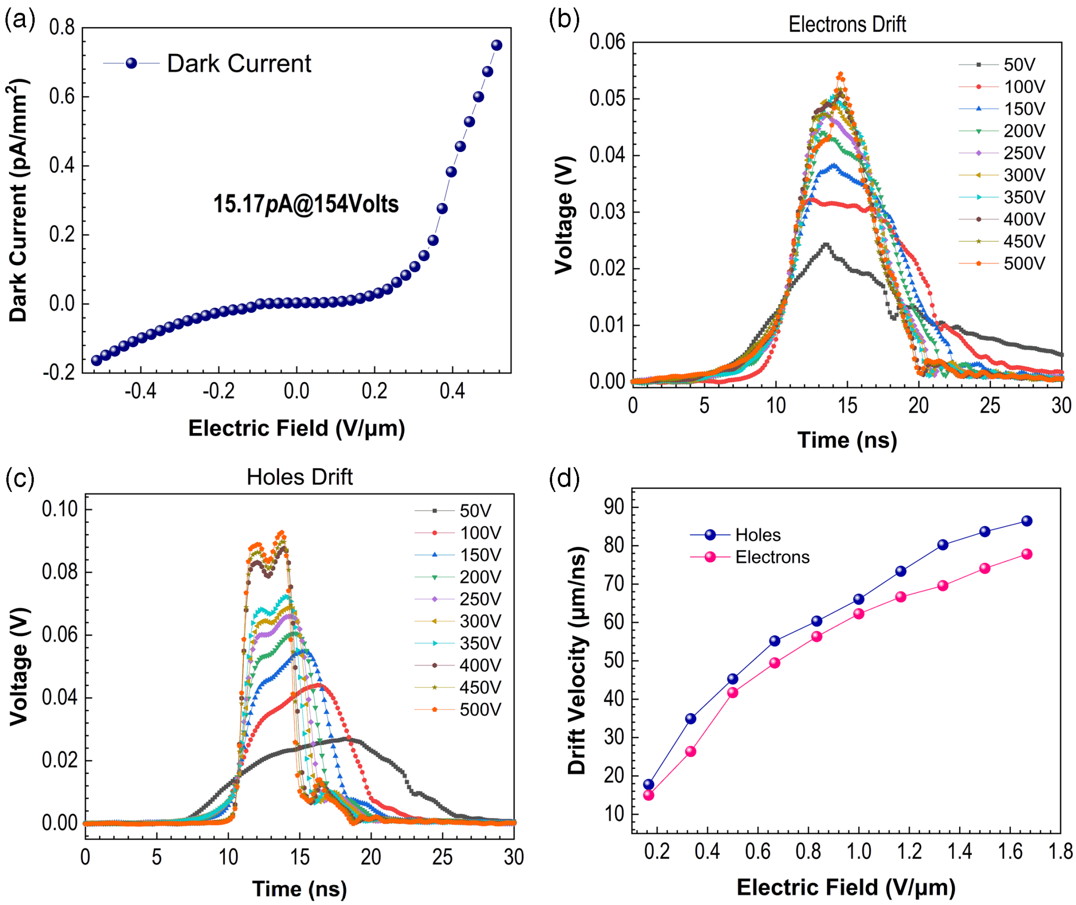

Figure 2. a) Dark current characteristics of the SCD detector. Bias-dependent time-resolved pulse response for b) electrons' and c) holes' drift. d) Carrier drift velocities as a function of the electric field applied on the SCD.

and holes could be calculated as 833.8 and 905.1 $cm^2V^{-1}s^{-1}$, respectively. The electric field-dependent drift velocities for the SCD detector are shown in Figure 2d. It can be observed that the drift velocity of carriers associated with the low electric field is approximately linear. As the electric field exceeds 1.0 V μm^{-1}, the upward trend slows down and gradually saturates up to 1.67 V μm^{-1}. As excessive bias voltage has little promotion effect on charge collection but rather produces a larger leakage current, which deteriorates the detector performance, the detector voltage was thereby fixed to 150 V. The CCE (η) of the SCD detector can be calculated by comparing its performance with a standard Si detector

$$\eta = \frac{P_{\mathrm{scd}} \cdot \varepsilon_{\mathrm{scd}}}{P_{\mathrm{Si}} \cdot \varepsilon_{\mathrm{Si}}} \tag{2}$$

where P_{scd} and P_{Si} are the peak positions of diamond detector and Si detector, respectively, whereas $\varepsilon_{\mathrm{scd}}$ and $\varepsilon_{\mathrm{Si}}$ are the ionization energies for diamond and Si, respectively (13.1 and 3.67 eV). The calculated CCEs of electrons and holes reach up to 99.2 and 98.8%, whereas their energy resolutions are 1.42 and 1.72%, respectively. The energy resolution of the SCD detector is better than that of the silicon detector under the same test conditions (Si: ≈1.89%). **Figure 3** shows the α-particle response spectra of the SCD detector and a silicon detector. These results lay the foundation for further study on particle identification algorithms.

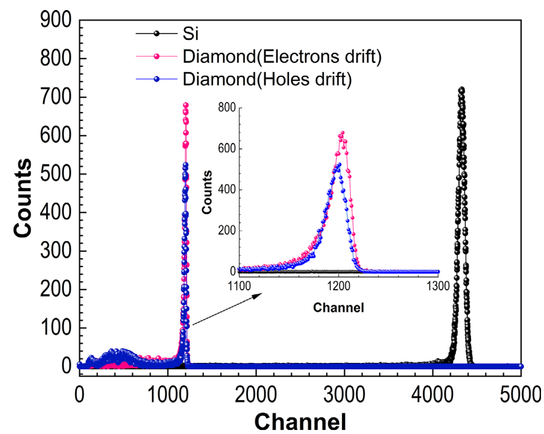

Figure 3. α-particle response spectra of the SCD detector and a silicon detector. A close-up view of SCD response spectra is shown in the inset.

In fact, the SCD detector's response to different particles varies significantly. For the α-particles, the response waveforms are rectangular as holes would take a finite time to travel from one side of the detector to the other. For a neutron event, the

© 2021 The Authors. Advanced Photonics Research published by Wiley-VCH GmbH

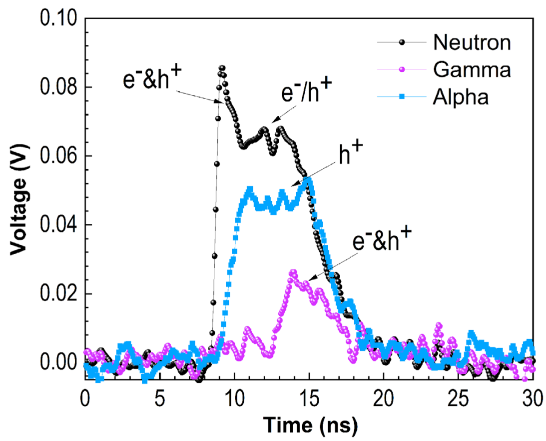

Figure 4. Time-dependent response waveforms of the SCD to the neutron, γ-ray, and α-particle radiation. The waveforms caused by drift of electrons (e^-) and holes (h^+) are marked in the figure.

generated carriers largely depend on the heavy charges produced during neutron energy deposition, which are greatly localized. Therefore, in the beginning of carrier migration, both the electrons and holes contribute to the current response, producing a sharp spike in the response waveforms. Once certain carriers (electrons or holes) reach the electrode, the leftover counterpart carriers continue to generate drift current, leading to a stepped response waveform. It is important to note that in a γ-ray event, as the Compton electrons were generated uniformly over the SCD, the "track-like" characteristic ionizations would produce uniform electron–hole pairs. The drifted carriers under bias contribute to the triangular waveform.[21] Examples of the three characteristic signals corresponding to a single neutron, γ-ray, and α-particle event are shown in **Figure 4**.

A 10 × 10 hexagonal topological space is defined, as shown in **Figure 5**a. Detailed modeling and coding for SOM algorithm can be found in Supporting Information, Part III. A series of signal preprocessing steps such as adjusting the baseline to zero, filtering, and aligning the peak among others is conducted for accurate and precise identification. After preprocessing, a 10 000 × 640 matrix composed of 5000 α signals from ^{238}Pu

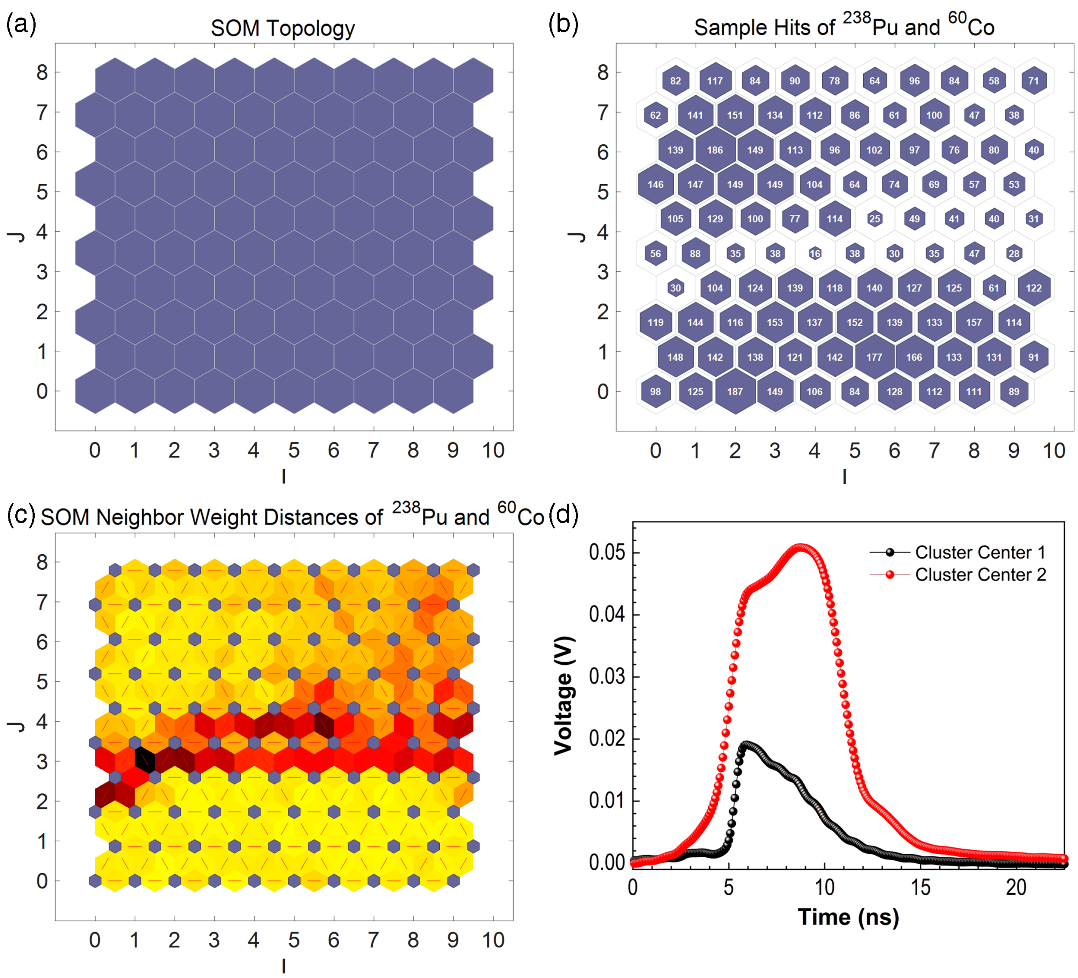

Figure 5. a) A 10 × 10 hexagonal SOM topological space. b) Sample hits of 10 000 α/γ signals in the neuron network clusters. c) SOM neighbor weight distances: larger distances are darker. d) Deep learning outcome of response pulses for ^{238}Pu α-particle (cluster center 1) and ^{60}Co γ-ray (cluster center 2) signals.

© 2021 The Authors. Advanced Photonics Research published by Wiley-VCH GmbH

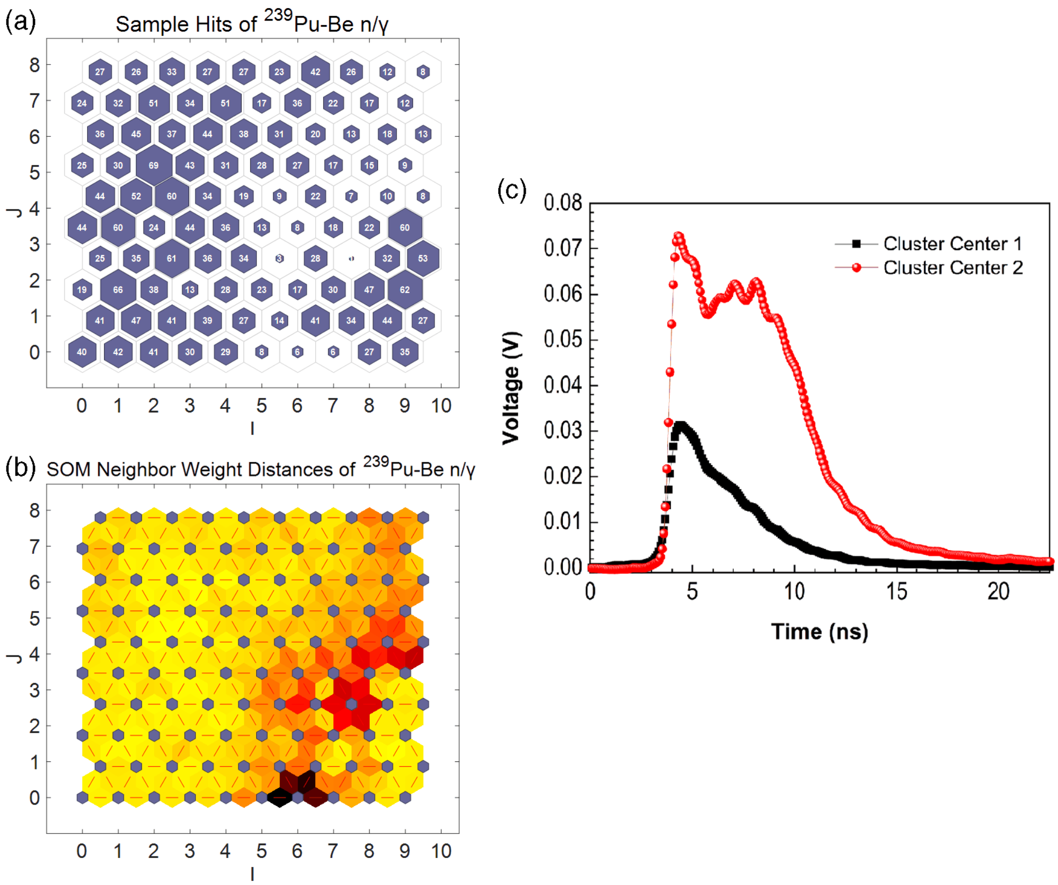

Figure 6. a) As-built topological sample hits of neuron networks for ^{239}Pu–Be neutron source, b) SOM neighbor weight distances, and c) deep learning outcome of response pulses for ^{239}Pu–Be neutron and γ-ray signals.

and 5000 γ signals from ^{60}Co is obtained. The said matrix can now be used to verify the accuracy of the proposed algorithm. A single signal output consists of 640 sampling points, which represent the voltage amplitude versus time with a sampling frequency of 12.8 GHz. Each signal in the matrix is mapped to the corresponding neuron after conducting 200 iterations with the SOM network, which means that all the 10 000 signals are labeled from 1 to 100. All signals are classified and the numbers of signals in each class are shown in Figure 5b. The number of hits within the regions of neurons represents the signals classified as the feature space. Figure 5c shows the Euclidian distance for each neuron's class away from its neighbors. Bright connections indicate highly connected areas of the input space, whereas the dark ones indicate regions of the feature space which are far apart, with few or no signals between them. Long borders of dark connections separating large regions of the input space indicate that the classes on either side of the border represent signals with very different features. It can be seen from Figure 5c that the signals are distinctly divided into two zones. The cluster centers of these two zones are shown in Figure 5d. Matching with the response waveforms in Figure 4, the cluster center 1 represents the γ-ray signals and cluster center 2 represents the α signals in Figure 5d. When validated against the manually labeled data, the SOM algorithm has an accuracy of 97.51% for pulse (α/γ) classification. Unlike other algorithms such as charge integration, the SOM algorithm needs no parameter optimization in advance for accurate recognition results.

Similarly, 3000 n/γ mixed signals are acquired with a ^{239}Pu–Be neutron source, which are mapped on a 10×10 network, as shown in **Figure 6**a. The mixed signals could also be broadly divided into two classes (see Figure 6b). The two cluster centers, namely, the cluster centers 1 and 2, are shown in Figure 6c, which represent the typical neutron and gamma pulse waveforms, respectively. The accuracy of n/γ separation based on SOM algorithm cannot be specifically estimated, as the 3000 n/γ signals are mixed and not labeled in advance. However, the distinct features of the two cluster centers in Figure 6c show how capable the SOM algorithm is in separating the n/γ signals.

3. Conclusion

A high-performance MSM SCD detector is developed and reported in this work with a low dark current density of about 0.75 pA mm^{-2} at a forward bias of 154 V. The TCT measurement implied that the CCE of the excited carriers saturates for an electric field higher than 0.5 V μm^{-1}, whereas the drift velocity gradually saturates up to 1.6 V μm^{-1}. Under the bias of 150 V, the

© 2021 The Authors. Advanced Photonics Research published by Wiley-VCH GmbH

response spectra of the SCD detector to ^{238}Pu α particles shows that the CCEs of up to 99.2 and 98.8% can be achieved for electrons and holes, with their energy resolution being as low as 1.42 and 1.72%, respectively. Enabled by a machine learning method based on SOM neural networks as a proof of concept, the SCD detector has demonstrated its potentials for accurate pulse shape discrimination. The proposed SOM algorithm achieves the accuracy of 97.51% when validated against the 10 000 manually labeled data (α/γ), while also effectively distinguishing the n/γ events simultaneously.

4. Experimental Section

A piece of Element-six (E6) electronic-grade SCD ($4.5 \times 4.5 \times 0.3$ mm^3) was used in this work. Raman characterization of SCD was conducted using a 532 nm pulse laser as the excitation source. A typical MSM detector was fabricated. For detector processing, the wafer was cleaned by piranha (a mixture of concentrated sulfuric acid with hydrogen peroxide in a ratio of 3:1 in volume) and aqua regia (a mixture of concentrated hydrochloric and nitric acid in a ratio of 3:1 in volume) solutions for 20 min to remove the organic contaminations and residual metals, respectively. After surface cleaning, Ti/Au (50 nm/200 nm) metal electrodes were deposited by an e-beam evaporator on both the sides of SCD separately. The sample was then loaded to a furnace and subsequently annealed in N_2 for 10 h at 800 °C to form good ohmic contacts. Finally, the detector was mounted on a self-designed printed circuit board (PCB) for wire bonding. For reducing the noise, the detector was encapsulated using coaxial subminiature version A (SMA) connector. The *I–V* characteristics were measured using a Keithley 4200 semiconductor parameter analyzer in the dark and in the electromagnetically shielded environment at room temperature. For more accurate results, the sweep delay time was set to 10 min due to the high resistivity of diamond. The TCT was used to measure the charge transport properties of the diamond detector, which can measure the fast current pulses generated from the drift of free carriers under the external electric field. The setup for the TCT measurements is shown in Figure S3 (Supporting Information). An α-particle source with energy of 5.25 MeV generated by ^{238}Pu (their penetration depth in diamond was less than 20 μm) was used to create carriers. Produced by either electrons or holes under different bias voltages, 1000 signals were collected. At a forward bias of 150 V, ^{238}Pu α-particle energy spectrum of the SCD detector was measured in a vacuum chamber and compared with that of the standard silicon detector to calculate the CCE of the SCD detector. Charge-sensitive preamplifier (Ortec 142AH) and digital multichannel analyzer (CAEN Hexagon) were used in the CCE measurement. The source was placed near the cathode and anode to acquire energy spectra due to electron drift and hole drift, respectively. SOM algorithm data analysis and landscape visualization were conducted using MATLAB (Mathworks) software. The n/γ mixed signals from ^{239}Pu–Be neutron source, α particle signals from ^{238}Pu, and γ-ray signals from ^{60}Co were sampled for the study of the discrimination algorithm.

Supporting Information

Supporting Information is available from the Wiley Online Library or from the author.

Acknowledgement

We acknowledge financial support from the Chinese Academy of Sciences.

Conflict of Interest

The authors declare no conflict of interest.

Data Availability Statement

The data that support the findings of this study are available from the corresponding author upon reasonable request.

Keywords

detectors, diamonds, machine learning, neural network algorithms, pulse shape discrimination, ultrawide-bandgap semiconductors

Received: May 20, 2021
Revised: August 15, 2021
Published online:

[1] M. Osipenko, M. Ripani, G. Ricco, B. Caiffi, F. Pompili, M. Pillon, M. Angelone, G. Verona-Rinati, R. Cardarelli, G. Mila, S. Argiro, *Methods Phys. Res. A* **2015**, *799*, 207.
[2] P. Weilhammer, W. Adam, C. Bauer, E. Berdermann, F. Bogani, E. Borchi, M. Bruzzi, C. Colledani, J. Conway, W. Dabrowski, P. Delpierre, A. Deneuville, W. Dulinski, R. V. D. Eijk, B. van Eijk, A. Fallou, D. Fish, M. Fried, K.K. Gan, E. Gheeraert, E. Grigoriev, G. Hallewell, R. Hall-Wilton, S. Han, F. Hartjes, J. Hrubec, D. Husson, H. Kagan, D. Kania, J. Kaplon, R. Kass, K.T. Knopfle, M. Krammer, P.F. Manfredi, D. Meier, L. L. S. Pan, *Nucl. Instrum. Methods Phys. Res A* **1998**, *409*, 264.
[3] J. Isberg, J. Hammersberg, E. Johansson, T. Wikström, D. J. Twitchen, A. J. Whitehead, S. E. Coe, G. A. Scarsbrook, *Science.* **2002**, *297*, 1670.
[4] C. Lee, C. Ban, H. Lee, K. Choo, B. Jun, *Appl. Radiat. Isot.* **2019**, *152*, 25.
[5] A. Tallaire, A. T. Collins, D. Charles, J. Achard, R. Sussmann, A. Gicquel, M. E. Newton, A. M. Edmonds, R. J. Cruddace, *Diam. Relat. Mater.* **2006**, *15*, 1700.
[6] H. Kagan, A. Alexopoulos, M. Artuso, F. Bachmair, L. Bäni, M. Bartosik, *Nucl. Instrum. Methods Phys. Res. A.* **2019**, *924*, 297.
[7] Y. Tzeng, C. C. Tin, R. Phillips, T. Srivinyunon, Y. Chen, *Appl. Phys. Lett.* **1990**, *57*, 789.
[8] F. H. Ruddy, A. R. Dulloo, J. G. Seidel, S. Seshadri, L. B. Rowland, *IEEE Trans Nucl Sci.* **1998**, *45*, 536.
[9] J. H. Ha, S. M. Kang, H. S. Kim, S. Park, N. H. Lee, T. Song, J. Kim, *J. Nucl. Sci. Technol.* **2011**, *1*, 237.
[10] V. Okhotnikov, S. Linnik, *Nucl. Instrum. Methods Phys. Res. A* **2019**, *936*, 686.
[11] G. Lutz, *Semiconductor Radiation Detectors*, Springer-Verlag Berlin Heidelberg, New York **2007**.
[12] W. U. Laub, T. W. Kaulich, F. Nüsslin, *Phys. Med. Biol.* **1999**, *44*, 2183.
[13] F. Schirru, K. Kisielewicz, T. Nowak, B. Marczewska, *J. Phys. D: Appl. Phys.* **2010**, *43*, 265101.
[14] M. Pillon, M. Angelone, A. Krása, A. J. M. Plompen, P. Schillebeeckx, M. L. Sergi, *Nucl. Instrum. Methods Phys. Res. A* **2011**, *640*, 185.
[15] K. Su, Z. Ren, J. Zhang, L. Liu, J. Zhang, Y. Zhang, Q. He, C. Zhang, X. Ouyang, Y. Hao, *Appl. Phys. Lett.* **2020**, *116*, 92104.
[16] K. Su, Q. He, J. Zhang, Z. Ren, L. Lin, J. Zhang, X. Ouyang, Y. Hao, *J. Phys. D: Appl. Phys.* **2021**, *54*, 145105.
[17] L. Bertalot, V. Krasilnikov, L. Core, A. Saxena, N. Yukhnov, R. Barnsley, M. Walsh, *J. Fusion Energ.* **2019**, *38*, 283.
[18] C. Cazzaniga, E. A. Sundén, F. Binda, G. Croci, G. Ericsson, L. Giacomelli, G. Gorini, E. Griesmayer, G. Grosso, G. Kaveney, M. Nocente, E. Perelli Cippo, M. Rebai, B. Syme, M. Tardocchi, *Rev. Sci. Instrum.* **2014**, *85*, 43506.
[19] C. Weiss, H. Frais-Kölbl, E. Griesmayer, P. Kavrigin, *Phys. J. A* **2016**, *52*, 269.

© 2021 The Authors. Advanced Photonics Research published by Wiley-VCH GmbH

[20] P. Kavrigin, P. Finocchiaro, E. Griesmayer, E. Jericha, A. Pappalardo, C. Weiss, *Nucl. Instrum. Methods Phys. Res. A* **2015**, *795*, 88.
[21] M. Passeri, D. Carnevale, B. Esposito, D. Marocco, S. Podda, F. Pompili, M. Riva, *Nucl. Instrum. Methods Phys. Res. A* **2020**, *974*, 164195.
[22] T. Kohonen, in *Proc. IEEE* **1990**, Vol. *78*, p. 1464.
[23] S. Ghorpade, J. Ghorpade, S. Mantri, *Int. J. Comput. Sci.* **2010**, *2*, 92.
[24] G. Wu, Q. Wang, Y. Wu, X. Sun, J. Liao, J. Pan, M. Chen, M. Kasu, S. Liu, *Today Commun.* **2020**, *25*, 101504.

 © 2021 The Authors. Advanced Photonics Research published by Wiley-VCH GmbH